J Adv Ceram

Research Article

The effect of nitrogen doping on the ablation resistance of zirconium carbide ceramics

Zheng Peng[1,†], Yingjie Cui[1,2,†], Jianbo Song[1], Sian Chen[1,✉], Zengsheng Ma[2,✉], Fuhua Cao[3,✉]

Cite this article: Peng Z, Cui Y, Song J, et al. *J Adv Ceram* 2025, **14**(5): 9221069. https://doi.org/10.26599/JAC.2025.9221069

ABSTRACT: Ultrahigh-temperature ceramics (UHTCs) are prominent candidates for use in thermal protection systems in the aerospace and nuclear industries. This study introduces a nitrogen-doped zirconium carbide that demonstrates remarkable ablation resistance, outperforming conventional carbide ceramics. The oxidation mechanisms of this material are elucidated through experimental and ab initio molecular dynamics simulations, representing the first analysis of such ultrahigh melting point ceramics from the perspective of structural development during the oxidation process. Transmission electron microscopy (TEM) analysis revealed the precipitation of nanocarbon and Zr–C–N–O phases at the interface between the oxidized and unoxidized regions following nitrogen doping. Nitrogen atoms preferentially combine with zirconium atoms at temperatures below the melting point of the oxide, forming robust Zr-C-N-O oxide network structures. These structures minimize oxide loss and maintain integrity during ablation, enhancing the material's performance in extreme environments. This study underscores nitrogen doping as a promising strategy to improve the ablation resistance of UHTCs, offering valuable insights for their application under demanding conditions.

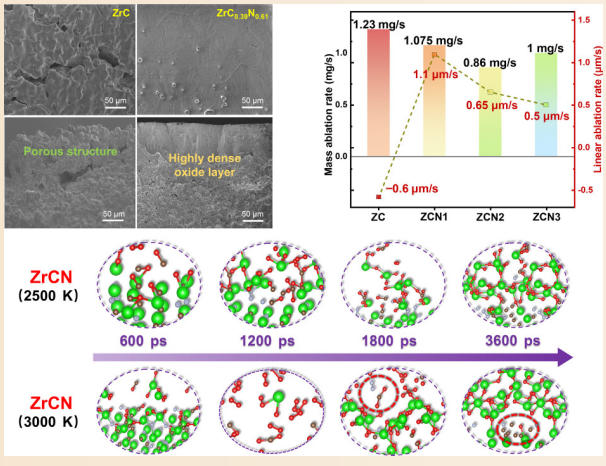

KEYWORDS: nitrogen doping; ultrahigh-temperature ceramics (UHTCs); ablation resistance; oxidation mechanisms; molecular dynamics simulations

1 Introduction

Ultrahigh-temperature ceramics (UHTCs), which include transition metal carbides, diborides, and nitrides, are notable for their ultrahigh melting points and are widely applied in thermal protection systems within the aerospace and nuclear industries [1,2]. Among these materials, zirconium carbide (ZrC) has garnered significant attention in recent years as a structural component of environments characterized by extreme erosion and high-temperature oxidation. This interest is attributed to its exceptional physical and chemical properties, which include relatively low density (6.59 g/cm^3), sufficiently high melting point (3540 °C), tendency to form refractory oxides [3,4], and cost-effectiveness [5]. However, carbides such as ZrC are prone to oxidation within the temperature range of 400–1200 °C, resulting in the formation of porous oxide films that fail to safeguard the material from further decomposition [6,7]. Consequently, for structural component materials intended for extreme environments, the development of single-phase ultrahigh-temperature ceramics that possess both self-healing capabilities and enhanced ablation resistance is essential.

Recent studies have indicated that solid solution mixtures composed of metal carbides and metal nitrides exhibit remarkable high-temperature stability and mechanical properties, which is attributed to the interplay of covalent, metallic, and ionic bonds [8–14]. The incorporation of nitrogen significantly enhances the oxidation resistance of carbides [15,16]. For example, while the initial oxidation temperature of ZrC ranges from 380 to 477 °C, zirconium nitride (ZrN) remains stable up to 900 °C without undergoing oxidation [13]. On the other hand, during the erosion assessment process, samples doped with nitrogen can form a dense oxide layer with a certain viscosity similar to that of the liquid silicate glass layers on the erosion surface, which plays an important role in preventing oxygen diffusion. Peng *et al.* [16]

† Zheng Peng and Yingjie Cui contributed equally to this work.

[1] Science and Technology on Advanced Ceramic Fibers and Composites Laboratory, College of Aerospace Science and Engineering, National University of Defense Technology, Changsha 410073, China. [2] School of Materials Science and Engineering, Xiangtan University, Xiangtan 411105, China. [3] School of Materials Science and Engineering, Central South University, Changsha 410083, China.

✉ Corresponding authors. E-mail: S. Chen, chensian07@nudt.edu.cn; Z. Ma, zsma@xtu.edu.cn; F. Cao, Caofuhua@csu.edu.cn

Received: January 19, 2025; Revised: February 16, 2025; Accepted: March 26, 2025

© The Author(s) 2025. This is an open access article under the terms of the Creative Commons Attribution 4.0 International License (CC BY 4.0, http://creativecommons.org/licenses/by/4.0/).

demonstrated through oxyacetylene experiments that nitrogen-doped hafnium carbide exhibited exceptional ablative resistance. A dense oxide layer forms on the ablated surface, effectively maintaining low oxygen permeability and retarding further oxidation of ultrahigh-temperature ceramics.

Given the complexities of the current situation, the high cost of hafnium-based ceramics is a serious problem in their preparation and application in the aerospace and other industries. However, zirconium-based ceramics, which are nearly ten times cheaper than hafnium-based powders are, are more suitable for practical application in current circumstances. However, related research on the nitrogen doping of zirconium carbide ultrahigh-temperature ceramics and their ablation resistance properties remains limited.

This study investigates a series of zirconium carbonitrides and elucidates the underlying ablative mechanisms via *ab initio* molecular dynamics simulations. Additionally, the composition and microstructural evolution of nitrogen-doped zirconium carbides during the ablation process at 3000 °C are demonstrated. Notably, the $ZrC_{0.39}N_{0.61}$ sample exhibited exceptional ablation resistance properties, positioning it as a promising candidate for applications in extreme environments.

2 Materials and methods

2.1 Synthesis and sintering

A tailored mixture of ZrCN powders with an average particle size of 1–3 μm and a purity of 99.5 wt% was prepared at a specific atomic ratio. The initial powder mixtures were subjected to ball milling and rotation at 300 r/min for 12 h in absolute ethanol, utilizing nylon pots and milling media. The ball-to-powder ratio was approximately 4 : 1. Following the milling process, the slurry was dried in an oven at 60 °C with forced convection air flow for 12 h. The prepared powders were subsequently consolidated via a spark plasma sintering furnace (FCT Systeme GmbH). The furnace was heated to 2000 °C under a pressure of 40 MPa, maintained for 10–20 min, and then cooled to room temperature under vacuum. Finally, ZrC_xN_y samples ($ZrC_{0.57}N_{0.43}$, $ZrC_{0.47}N_{0.53}$, $ZrC_{0.39}N_{0.61}$, and $ZrC_{0.28}N_{0.72}$) with a diameter of 28 mm were prepared. For comparison, a pure ZrC sample was prepared via the same method.

The elemental composition of the consolidated sample was analyzed via electron probe microanalysis (EPMA), as presented in Table 1. A minor presence of oxygen impurities was identified, which were attributed to the raw materials or oxidation during the grinding and sintering processes.

2.2 Ablation experiment

The ablation experiment was conducted via an oxyacetylene torch system in accordance with the GJB 323A-96 standard. The flow rates of oxygen and acetylene were set at 1512 and 1116 L/h, respectively, while the pressures for oxygen and acetylene were maintained at 0.400 and 0.095 MPa, respectively. The sample was subjected to an oxyacetylene flame for a duration of 200 s. During this experiment, the optical pyrometer indicated that the maximum temperature of the central ablative surface reached approximately 2500 °C. The mass ablation rate (MAR) and linear ablation rate (LAR) were calculated via the formulas $R_m = \Delta m/t$, and $R_l = \Delta l/t$, respectively where R_m denotes the MAR, R_l denotes the LAR, Δm represents the decrease in mass, Δl indicates the length loss of the sample, and t refers to the duration of ablation. Changes in weight and thickness during ablation were recorded via an electronic balance and a Vernier scale.

Table 1 Elemental analysis of consolidated ZrC and ZrC_xN_y samples via EPMA (Unit: at%)

Sample ID		Composition				Total
		Zr	C	N	O	
ZC	ZrC	50.32	46.95	—	2.73	100.00
ZCN1	$ZrC_{0.63}N_{0.37}$	56.48	26.76	15.51	1.24	99.99
ZCN2	$ZrC_{0.47}N_{0.53}$	55.21	20.61	23.03	1.14	99.99
ZCN3	$ZrC_{0.39}N_{0.61}$	53.43	17.90	27.17	1.50	100.00
ZCN4	$ZrC_{0.28}N_{0.72}$	50.82	13.53	33.82	1.83	100.00

2.3 Characterizations

The phase characterization was conducted via an X-ray diffractometer (XRD; Smartlab SE, Empyren). The density of the bulk material was determined through the Archimedean drainage method. The relative density of each sample was calculated from the measured density and theoretical density, which was derived from the ideal stoichiometry and lattice parameters obtained from XRD. The microstructures of the sample surfaces were analyzed by scanning electron microscopy (SEM; Regulus 8100, Hitachi), which was equipped with an energy-dispersive X-ray spectrometer (EDS). Additionally, the detailed elemental distribution was characterized via transmission electron microscopy (TEM; F200, JEOL).

2.4 *Ab initio* molecular dynamic simulation

A quasirandom ZrCN phase supercell containing 196 atoms was generated via a Monte Carlo (MC) algorithm implemented in the Alloy Theoretic Automated Toolkit (ATAT) developed by Alex van de Walle *et al.* [17]. The ZrC supercell, which also contains 196 atoms, was generated on the basis of its well-defined crystal structure and atomic occupancy. Brillouin zone integrations were performed via 3 × 3 × 1 Monkhorst–Pack *k*-point grids. In the energy minimization process, the structures were optimized until convergence occurred, and the SCF convergence thresholds were less than 0.01 eV/Å and 1×10^{-5} eV/atom. The (001) surfaces were generated by introducing a vacuum space of 15 Å at the cleavage plane layers. A total of 33 O_2 molecules were distributed randomly to fill the vacuum space, resulting in a sufficient concentration of O_2 to reach the deepest layer at the O_2–ZrCN/ZrC interfaces. Born Oppenheimer AIMD simulations of O_2–ZrCN/ZrC models are carried out at 2500 K within the NVT ensemble using the NoséHoover thermostat for 10 ps. The two bottom monolayers were kept frozen to mimic the bulk constraint. The AIMD simulations were performed via the Vienna *Ab initio* Simulation Package (VASP) [18–20], which employs a projector augmented wave (PAW) method [21] to handle electron–ion interactions. The exchange and correlation interactions were described by a gradient-corrected functional in the Perdew–Burke–Ernzerhof (PBE) [22] form. A high energy cutoff of 500 eV was employed for plane-wave basis set expansion. During the simulations, the equations of motion were integrated with a timestep of 1 fs, and forces were calculated via *Γ*-point sampling.

3 Results and discussion

3.1 Structural characterizations of nitrogen-doped zirconium carbide

Figure 1(a) shows the XRD patterns of the zirconium carbonitride samples with different compositions. The results indicate that the

consolidated samples have achieved solid solutions with a single-phase structure, which are characterized by face-centered cubic (FCC) lattices. Figure 1(b) clearly shows that as the composition changes, the diffraction peaks progressively shift to higher angles than those of the pure ZrC sample. This shift signifies lattice contraction resulting from the partial substitution of carbon atoms by nitrogen in the sublattice. According to Vegard's law [23], the relationship between the lattice constant of carbonitrides and the C/(C+N) ratio is based on Eq. (1):

$$\bar{a}_{x\to y} = a_x C_x + a_y (1 - C_x) \quad (1)$$

where $a_{x\to y}$ is the lattice constant of ZrC_xN_y, a_x is the standard lattice constant of ZrC, a_y is the standard lattice constant of ZrN, and C_x is the average content of carbides in the solidified sample. Figure 1(c) shows the experimentally measured and theoretically calculated lattice constants of the carbonitrides in accordance with Vegard's law. As shown in the figure, the unit cell parameter of zirconium carbide is 4.698 Å, that of the zirconium nitride crystal is 4.585 Å, and the ZrC_xN_y lattice parameters are between 4.585 and 4.698 Å. This result confirms that the lattice parameters decrease following the replacement of carbon atoms with nitrogen atoms in the ZrC system.

SEM characterization revealed the microstructures of the ZrC and ZrC_xN_y systems. Many pores are clearly observed on the surfaces of the ZC (Fig. 2(a)) and ZCN1 (Fig. 2(b)) samples. Conversely, the ZCN2, ZCN3, and ZCN4 samples have dense microstructures, as evidenced in Figs. 2(c)–2(e). Additionally, the comparison of the ZC and ZCN1 samples indicates that the grain size increases with increasing nitrogen doping. This could be attributed to active recrystallization during the consolidation process in the ZrC_xN_y system [24]. Moreover, the reduction in pore size may be related to the increased diffusion mobility of crystal defects [24,25]. The relative density curves with varying compositions (Fig. 2(f)) show that ZC and ZCN1 have lower relative densities (89.06% and 91.10%, respectively) in the presence of pores, whereas ZCN2, ZCN3, and ZCN4 exhibit higher relative densities (98.67%, 98.32%, and 97.92%, respectively) without noticeable pores. Furthermore, the elemental mappings clearly demonstrate a uniform distribution of elements in ZCN3 with no apparent element segregation, confirming the uniform composition distribution at the micrometer scale.

To further investigate the crystal structure at the nanoscale, TEM analysis was performed. Figure 3(a) shows a representative high-resolution transmission electron microscopy (HRTEM) image of ZCN3, which reveals a distinct periodic lattice structure characterized by stripes that are approximately 0.267 nm apart. This spacing corresponds to the *d*-spacing of the (111) plane in the FCC structure. The calculated lattice parameter is approximately 4.625 Å, which closely aligns with the XRD result of 4.626 Å. Moreover, selected area electron diffraction (SAED) along the [011] axis also confirmed that ZCN3 possesses a typical FCC carbonitride structure, as shown in Fig. 3(b). The corresponding elemental map shows that Zr, C, and N are uniformly distributed at the nanometer scale, as shown in Fig. 3(c).

3.2 Ablation performance and morphology of nitrogen-doped zirconium carbide

The morphology of the ZrC and ZrC_xN_y samples before and after

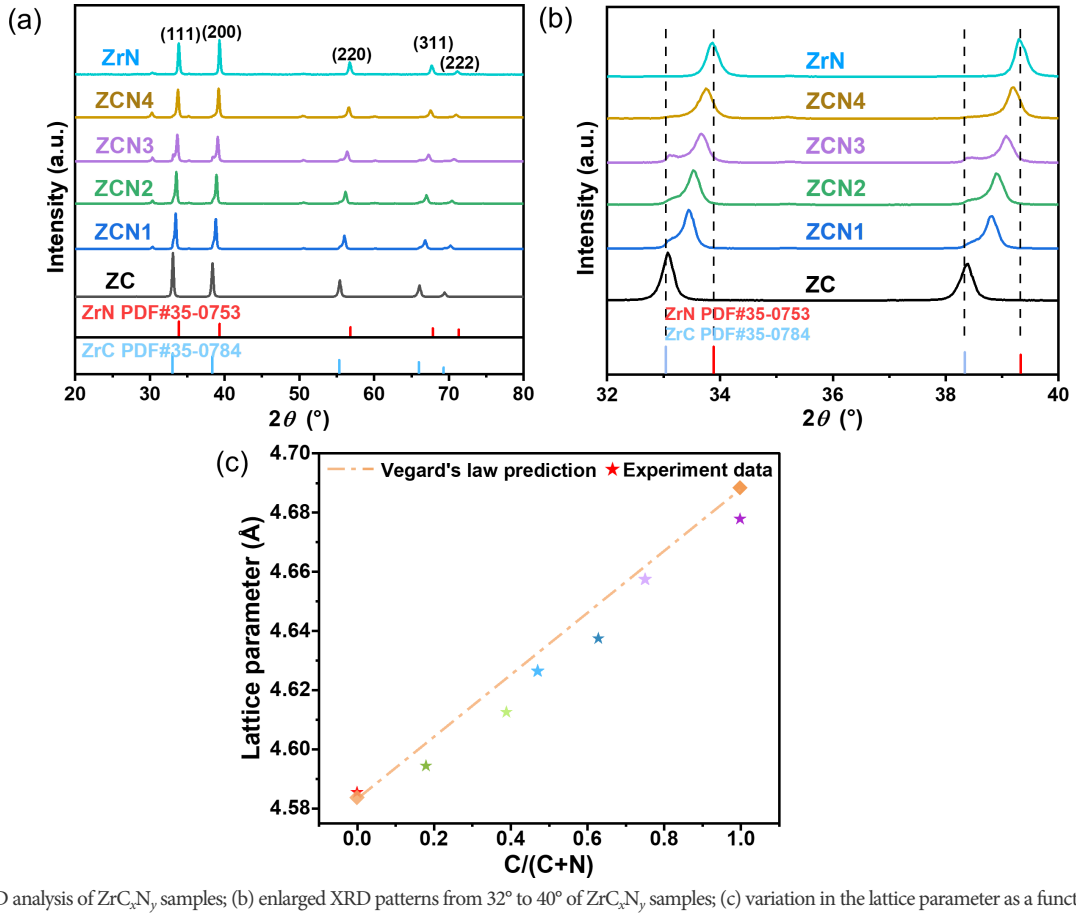

Fig. 1 (a) XRD analysis of ZrC_xN_y samples; (b) enlarged XRD patterns from 32° to 40° of ZrC_xN_y samples; (c) variation in the lattice parameter as a function of the C/(C + N) ratio.

清華大学出版社 Tsinghua University Press | SciOpen

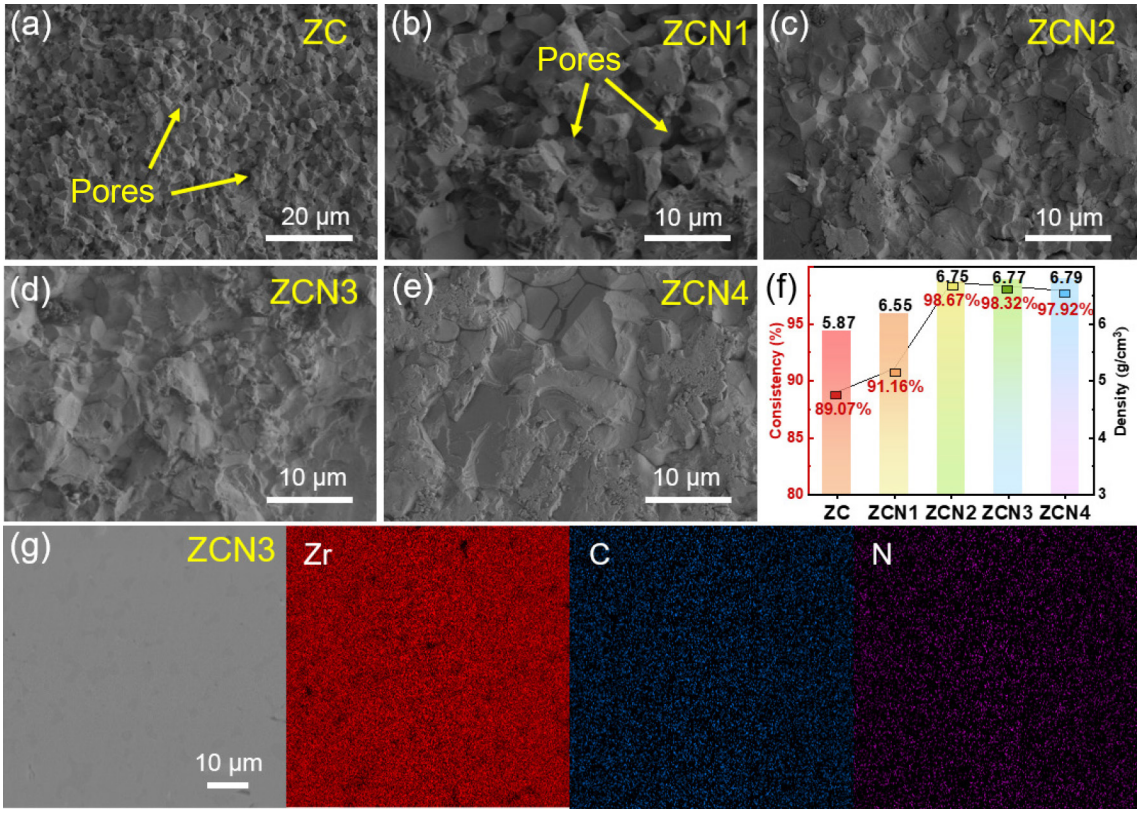

Fig. 2 SEM images of surface microstructures in (a) ZC, (b) ZCN1, (c) ZCN2, (d) ZCN3, and (e) ZCN4. (f) Density and relative density curves of ZrC_xN_y. (g) Elemental mappings of ZCN3 via EDS.

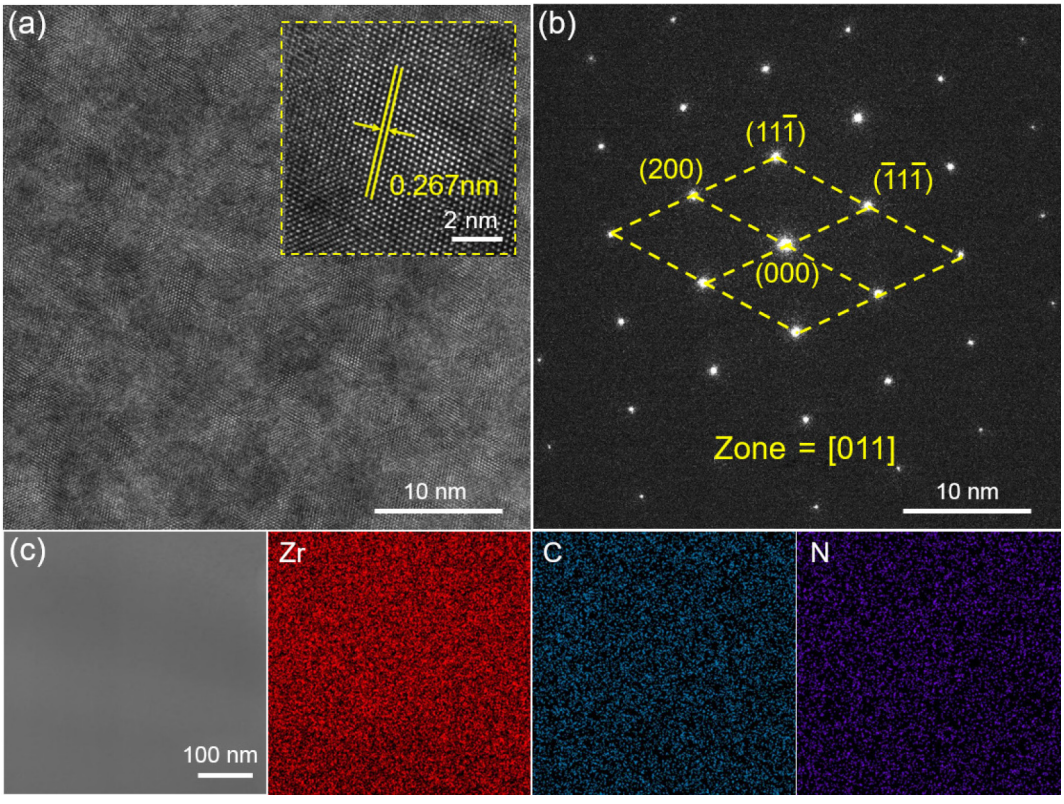

Fig. 3 (a) High-resolution transmission electron microscope image of ZCN3 (the insert is an inverse Fourier transform (IFFT) image); (b) electron diffraction pattern of ZCN3; (c) STEM images and corresponding EDS mappings of ZCN3.

the ablation tests is illustrated in Fig. 4(a). Optical observations of the initial samples revealed a distinct color transition from dark gray to light gray, which ultimately shifted to purplish red. This progression corresponds to variations in nitrogen content and reflects changes in reflectance due to electron density [26]. To evaluate the practical application potential at ultrahigh

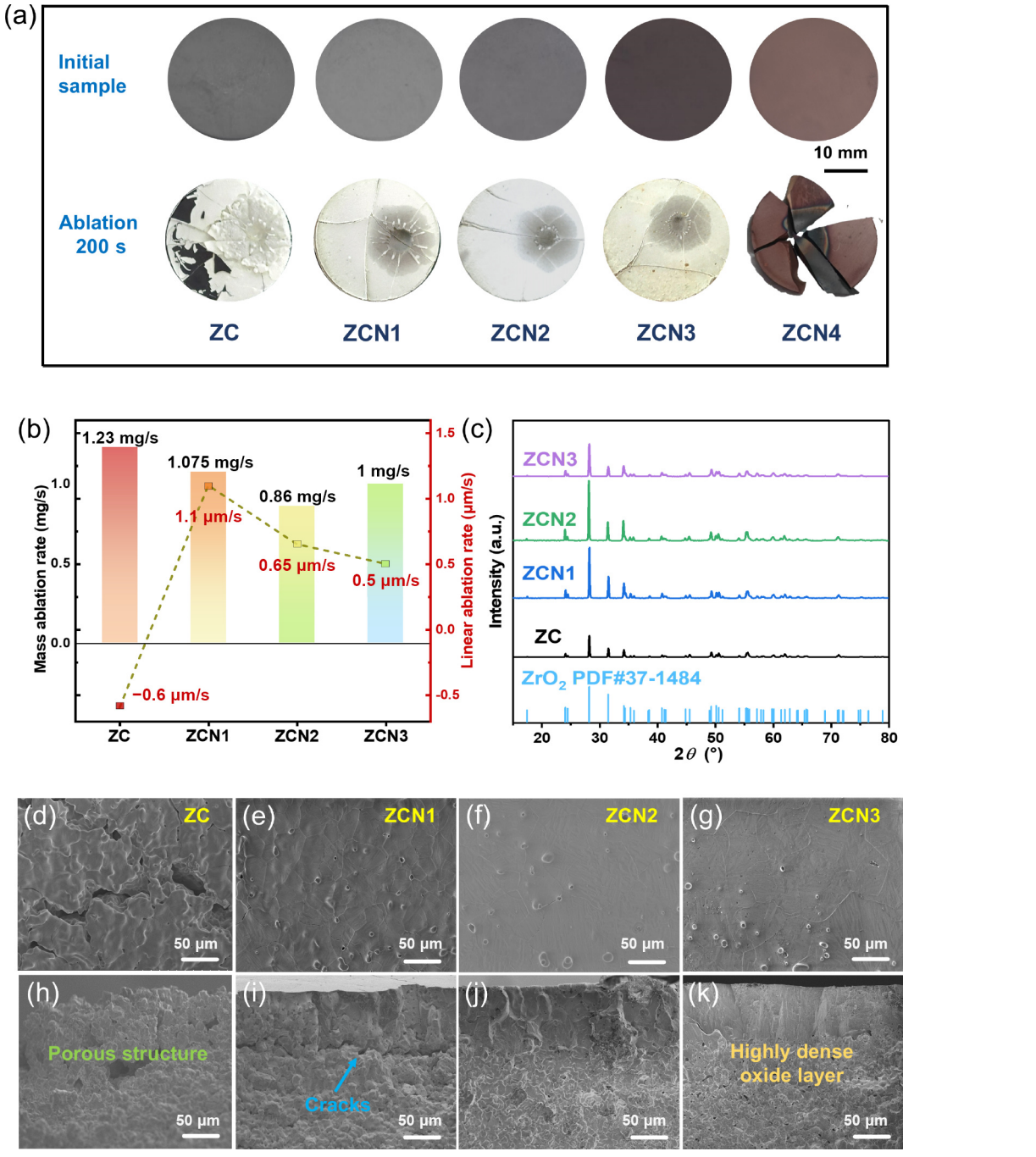

Fig. 4 (a) Morphology of ZrC_xN_y samples before and after ablation process; (b) linear and mass ablation rates of ZrC_xN_y solid solutions at 3000 °C for 200 s; (c) XRD analysis of ablated samples on the surface. Lines of black, blue green and purple represent ablated ZC, ZCN1, ZCN2, and ZCN3 samples, (d–g) Surface ablated microstructures of ZrC and ZrC_xN_y, (h–k) Cross-section ablated microstructures of ZrC and ZrC_xN_y.

temperatures, the antiablation properties of these ultrahigh-temperature compounds were tested via an oxyacetylene flame with a heat flux of 4.1 MW/m^2. The combined effects of thermal erosion, oxidative reactions, and mechanical denudation from the oxyacetylene flame are reflected in the ceramic samples.

The surface of the ZC sample shows significant erosion with substantial peeling of the oxide scale. In contrast, the ZrC_xN_y samples remain intact without peeling during ablation, which illustrates that the incorporation of nitrogen enhances the bonding of the oxide layer with the underlying nonoxide matrix. Additionally, droplet-like substances diffusing outward from the ablation center are observed in the morphologies of the ZCN1, ZCN2, and ZCN3 samples. This phenomenon demonstrates that the melt during ablation has a certain viscosity and fluidity, as observed in silicon-based oxide glass [27–35]. Moreover, a comparative analysis indicates that as the nitrogen content increases, the extent of outward sputtering from the central ablation area progressively diminishes, suggesting the increase in viscosity in the molten phase. Furthermore, the number of central ablation pits on the surfaces of the ablated samples decreases as the nitrogen content increases. However, the ZCN4 sample, which has a relatively high nitrogen content compared with the other samples, failed to withstand the high-speed oxyacetylene torch and exhibited fatal damage.

Figure 4(b) shows the mass ablation rate and linear ablation rate of these materials, which represent the ablation losses per unit

time. Generally, a higher MAR or LAR value indicates a more rapid loss of material quality. A comprehensive comparison of the mass ablation rate and line ablation rate reveals that the ablation performance of ZCN3 is the best among these samples. The primary phase identified in the oxide layer is ZrO_2 (PDF#37-1484) by XRD analysis, as shown in Fig. 4(c). This finding indicates that the sample surface was completely oxidized under the oxyacetylene flame at 3000 °C.

To understand the ablation resistance, the ablated surface and cross-sectional microstructures of the ZrC_xN_y samples were analyzed by scanning electron microscopy (SEM) (Figs. 4(d)–4(k)). Unlike the porous ablation structure of ZC (Fig. 4(d)), which exhibited numerous pores and defects, the series of ablated ZCN samples (Figs. 4(e)–4(g)) formed a dense oxide layer. The compactness of the oxide layer in nitrogen-doped zirconium carbide can be attributed to the suitable viscosity of the molten material at ultrahigh temperatures. This characteristic effectively seals defects such as pores and cracks, thereby preventing further oxygen infiltration into the substrate. The observation of a bubble-like morphology on the surface of the ablated sample (Figs. 4(e)–4(g)) further supports this conclusion.

The ablated cross-sectional microstructures of the ZrC_xN_y samples are presented in Figs. 4(h)–4(k). Notable differences could be observed in the ablated cross-section characterization. Figure 4(h) shows the ablated cross-section of the ZC sample, which predominantly displays a porous oxide morphology. The external oxide layer detached, with large cracks between the middle layer and the inner matrix (Fig. 4(h)). The oxide layer appears relatively dense without pores for the ablated ZCN1, ZCN2, and ZCN3 samples. However, there is a thermal expansion coefficient mismatch in the oxide layer for the ZCN1 sample with a low nitrogen content.

To further investigate the discrepancy in ablated morphology among various samples, a detailed and comprehensive characterization of the ablated cross-sectional microstructure is conducted. The cross-sectional microstructures at high magnifications can be categorized into four distinct layers: the dense outer layer, the middle layer characterized by a fine particle size, the tightly structured inner layer, and the ceramic matrix. The variations in the morphology of the oxide layer may be attributed to the thermal gradient, oxygen partial pressure gradient [36], and residual nitrogen content in each region. Generally, a dense surface layer can act as an antioxidant barrier, thereby minimizing oxide loss and optimizing ablation performance. Figures 5(a)–5(c)

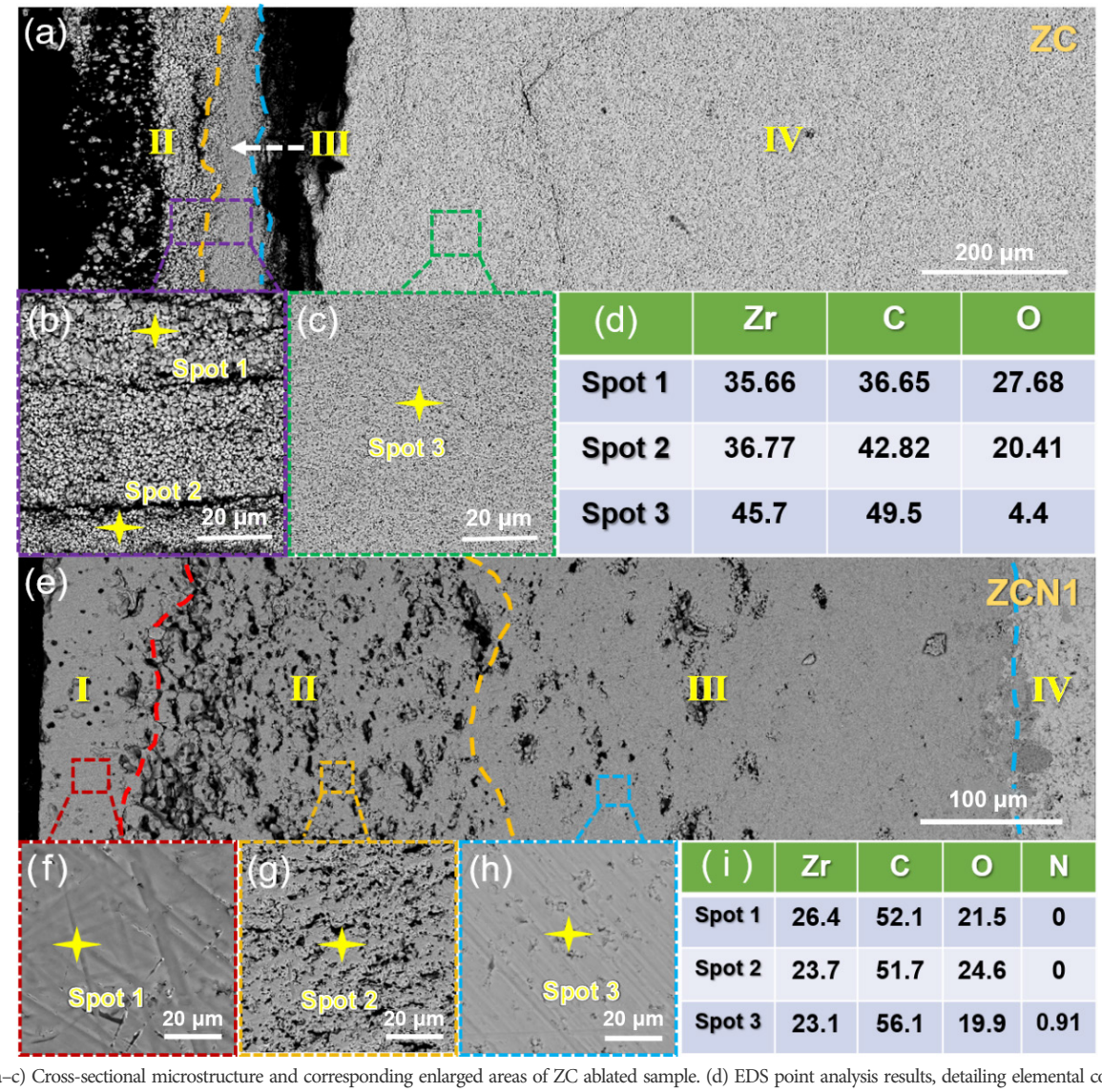

Fig. 5 (a–c) Cross-sectional microstructure and corresponding enlarged areas of ZC ablated sample. (d) EDS point analysis results, detailing elemental composition within enlarged cross-section of ZC sample. (e–h) Cross-sectional microstructure and corresponding enlarged areas of ablated ZCN1 sample. (i) EDS point analysis results, which show the elemental composition within the enlarged cross-section of ZCN1 sample.

show the ablated ZC cross-sectional microstructures. The resin-prepared cross section reveals that the surface oxide layer has peeled away. Some fine particles within the intermediate layer detached due to mechanical forces during the grinding and polishing processes, and the inner layer separated from the matrix. In contrast, no significant cracks are observed in the nitrogen-doped zirconium carbide samples following the ablation experiment (Figs. 5(e)–5(h)). Notably, the ablated ZCN1 sample reveals that the inner layer within the oxidized region strongly adheres to the matrix. However, the external oxide region in low nitrogen-doped zirconium carbide (ZCN1) retains considerable porosity after ablation. These microstructures accelerate the oxidation of the matrix, leading to excessive oxide thickness. Additionally, large pores also exist between the external and middle layers, which results in the detachment of oxide scales.

Figure 6 presents the cross-sectional microstructures and morphologies of the ablated ZCN2 and ZCN3 samples. These observations indicate that as the nitrogen content increases, the particle size and pore size within the middle layer gradually decrease, particularly those adjacent to the ablation surface. The inner layer demonstrates commendable adaptation with the substrate for the ZCN2 and ZCN3 samples. Moreover, the oxygen content in each region decreases as the longitudinal depth increases. EDS point analysis indicates that the ZCN1 sample lacks nitrogen in the outermost oxidation zone, leading to the oxidation of the outer micropores and the subsequent formation of larger particles and pores within the middle layer. Conversely, as the nitrogen content increases, the residual nitrogen in each oxidation zone gradually increases after the ablation process. Comparative research indicates that the presence of nitrogen can significantly mitigate the mismatched thermal expansion coefficients between the oxide layer and substrate, as evidenced by the compact ablated morphology.

To investigate the phenomenon between the oxide layer and the nonoxide region with nitrogen doping, focused ion beam (FIB) slices from region three in ZCN3 were extracted to characterize the microstructures at the nanoscale. As depicted in Fig. 7(a), TEM analysis was performed on the regions highlighted in red. The TEM image reveals several regions with distinct compositions, designated regions I, II, III, and IV. EDS analysis of the selected area revealed significant differences in the elemental distribution, as depicted in Fig. 7(g). Notably, the regions I and IV predominantly consist of carbon; however, a distinct difference between the two regions is clearly visible in the TEM image. Therefore, high-resolution images of both regions and their fast Fourier transform (FFT) patterns are studied. The region I is

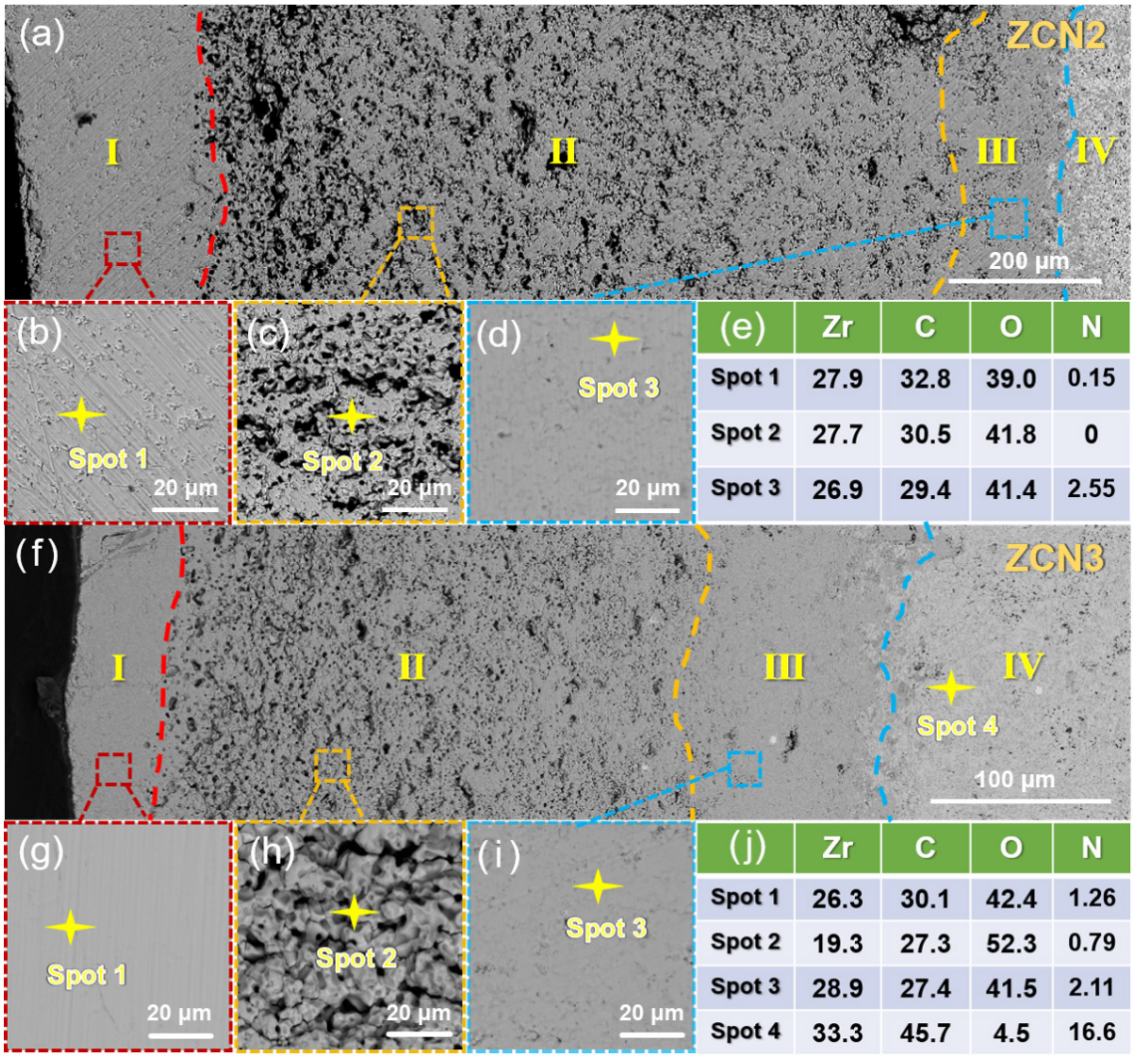

(e)	Zr	C	O	N
Spot 1	27.9	32.8	39.0	0.15
Spot 2	27.7	30.5	41.8	0
Spot 3	26.9	29.4	41.4	2.55

(j)	Zr	C	O	N
Spot 1	26.3	30.1	42.4	1.26
Spot 2	19.3	27.3	52.3	0.79
Spot 3	28.9	27.4	41.5	2.11
Spot 4	33.3	45.7	4.5	16.6

Fig. 6 (a–d) Cross-sectional microstructure along with the corresponding enlarged areas of ablated ZCN2 sample. (e) EDS point analysis results, detailing elemental composition within enlarged cross-section of the ablated ZCN2 sample. (f–i) Cross-sectional microstructure and the corresponding enlarged areas of ablated ZCN3 sample. (j) EDS point analysis results, which detail elemental composition within enlarged cross-section of ablated ZCN3 sample.

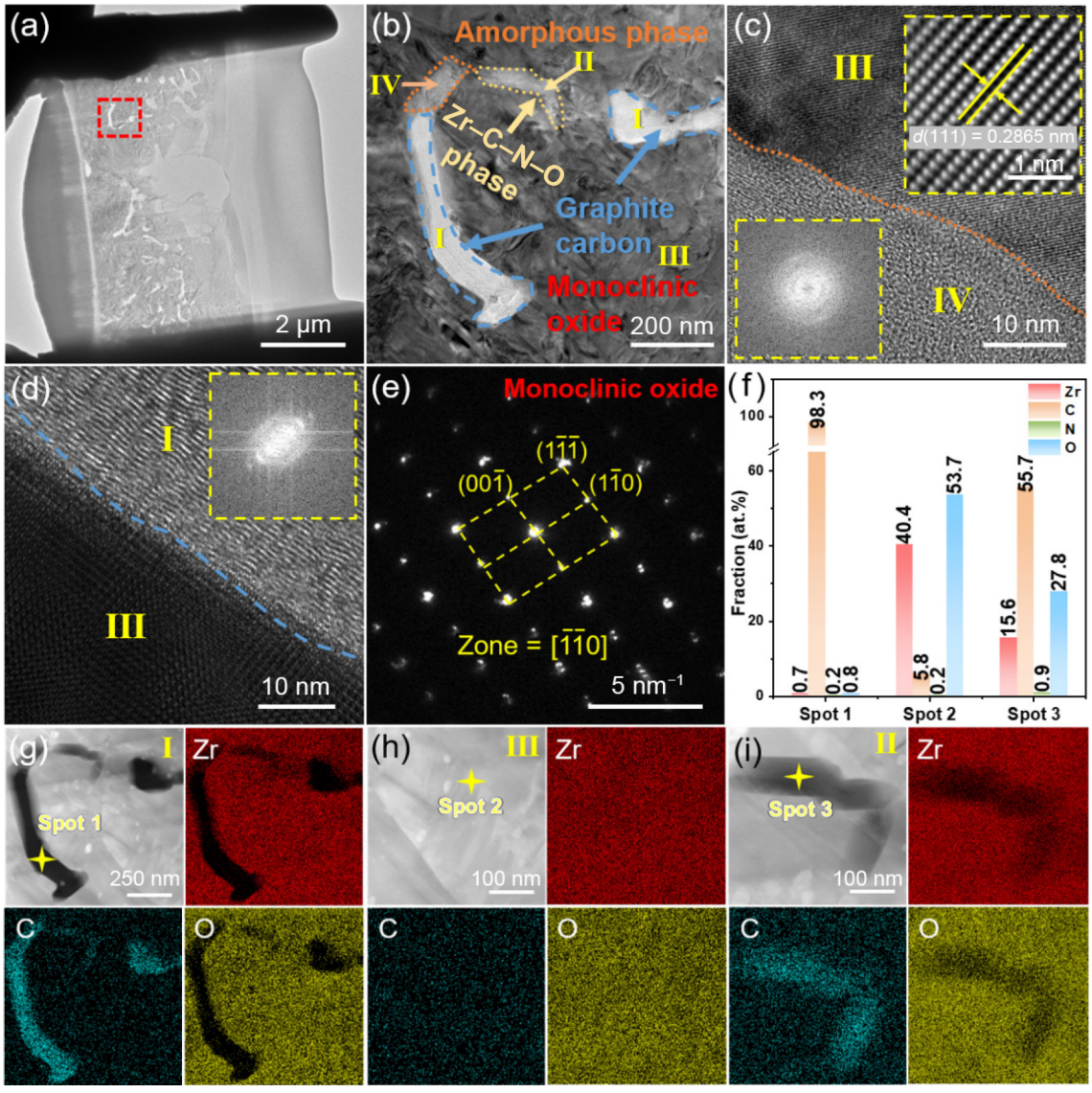

Fig. 7 (a) HAADF-STEM image of oxidized region at inner layer of ZCN3; (b) magnified TEM image of region in (a); (c, d) high-magnification images of the boundaries between region III and region IV, as well as region I and region III in (b), respectively, with the corresponding FFT mode images inserted; (e) electron diffraction pattern of monoclinic oxide; (f) ratio of element content of spots 1–3; (g) distribution of related elements in (b); (h, i) local enlarged views of region 2 and region 3 as well as associated distribution of elements.

identified as layered graphite structure carbon, whereas region IV is amorphous carbon. This indicates that carbon precipitation occurred during the ablation process, suggesting a transition between amorphous carbon and layered graphite. According to Fig. 7(e), the oxide in the region III is identified as monoclinic zirconia, which aligns with the energy spectrum analysis results obtained through transmission electron microscopy (Figs. 7(f) and 7(h)). The region II underwent energy spectrum surface scanning and point scanning, confirming that the material in this region is a Zr–C–O phase, which also contains a certain amount of nitrogen. This phase demonstrates good compatibility with zirconia, effectively addressing the issue of mismatched thermal expansion coefficients between the monoclinic oxide and the face-centered cubic matrix.

3.3 Ablation resistance mechanisms of nitrogen-doped zirconium carbide

On the basis of the analysis of ablation resistance performance and ablated microstructures, nitrogen-doped zirconium carbide exhibited superior ablation resistance capabilities compared with those of pure zirconium carbide. An illustration of the ablation mechanism at the microscale reveals that, in contrast to the porous and loose microstructures of ablated zirconium carbide, a dense oxide layer forms on the surface of the nitrogen-doped zirconium carbides during ablation at 3000 °C. This protective layer plays a crucial role in inhibiting the infiltration of oxygen at ultrahigh temperatures. Generally, the diffusion rate of oxygen through pores or cracks is significantly higher than that through solid materials. Consequently, the porous and loose ablation structures can lead to further oxidation of the matrix [37].

On the other hand, a dense oxide layer with suitable viscosity can significantly mitigate the loss of oxides during assessment. References [9,38] indicate that nitrogen-containing oxides demonstrate a substantial increase in viscosity. Notably, our research results indicate that a significant increase in oxide viscosity is correlated with nitrogen doping in the carbide lattice. Under mechanical scouring and ablation conditions, the viscosity of the liquid phase plays a critical role in system performance. The molten phase can be retained within the system to effectively seal

pores and repair microcracks, thereby establishing a protective barrier that significantly inhibits oxygen diffusion toward the substrate material. Notably, after the ablation test, the increase in the nitrogen content in nitrogen-doped zirconium carbide resulted in a decreased sputtering range and a reduction in the porosity of the dense oxide layer. The suitable viscosity of oxides is crucial for resisting chemical and mechanical erosion and offers great protection under ultrahigh-temperature ablation conditions.

To further investigate the oxidation process of nitrogen-doped zirconium carbide and its enhanced ablation resistance performance, ab initio molecular dynamics simulations were conducted to elucidate the underlying oxidation resistance mechanism. Considering that oxygen must first interact with the surface of the oxide layer during the ablation process, we established a vacuum layer on the surface of the supercell and randomly distributed oxygen atoms within it. Figure 8 presents schematic diagrams of ZrC and ZrCN at various time points during the oxidation process under different temperature conditions. For the ZrC sample, the transient image at 600 ps reveals that oxygen atoms interact with surface atoms to form bonds, resulting in the generation of carbon monoxide (CO) and zirconium carbon monoxide (ZrCO). CO subsequently detaches from the surface of the oxide layer with pores. At the same time, carbon atoms are released from the surface layer, which allows oxygen atoms to penetrate into the second layer and form bonds with Zr atoms. This process leads to porous ablated structures of zirconium carbide, which promotes the reaction between oxygen and the internal matrix. As the oxidation time increases, the surface layer atoms react with oxygen to produce ZrO_x, CO, and CO_2, which subsequently detach from the surface layer. These simulation results account for the phenomenon of oxide peeling observed in the ZC sample.

Moreover, instantaneous images of nitrogen-doped zirconium carbide at different time intervals are presented under 2500 and 3000 K temperature fields. During the initial period of 0–1800 ps, oxygen atoms predominantly form bonds with zirconium and carbon atoms. Concurrently, the ZrO_2 phases partially detached from the surface of the oxide layer. The early oxidation stages for nitrogen-doped zirconium carbide exhibit striking similarities to those of pure zirconium carbide. As the oxidation process continues, the robust bonding between nitrogen and zirconium atoms hinders the detachment of oxide from the surface layer, resulting in the formation of a network structure. This characteristic aligns with the suitable viscosity of the oxide layer and reduces the loss of oxides during the ablation process, as discussed previously. Notably, under a 2500 K temperature field, nitrogen atoms predominantly reside within the oxide network structure, forming stable bonds with Zr atoms. This configuration enhances the structural integrity of the oxide layer, thereby delaying oxide detachment and the release of CO/CO_2. In contrast, under the 3000 K temperature field, nitrogen is progressively released in the form of N_2 gas without disrupting the integrity of the network structure. Additionally, a small aggregation of carbon atoms can be detected at 3600 ps at 3000 K. This phenomenon of carbon precipitation during the ablation process is also observed in the literature [39,40], which may be related to the preferential oxidation of zirconium atoms [39–42]. The AIMD simulations reproduce essential processes derived from experiments, providing atomic-level validation for the improved thermostability and ablation resistance of ZrCN.

Nitrogen has essential functions in the ablation resistance mechanism of nitrogen-doped zirconium carbide. First, nitrogen doping increases the viscosity of the oxide layer. This change helps form a dense oxide barrier, effectively blocking the flow of oxygen through pores or cracks to the substrate. Second, the robust bonding interactions between nitrogen and zirconium atoms

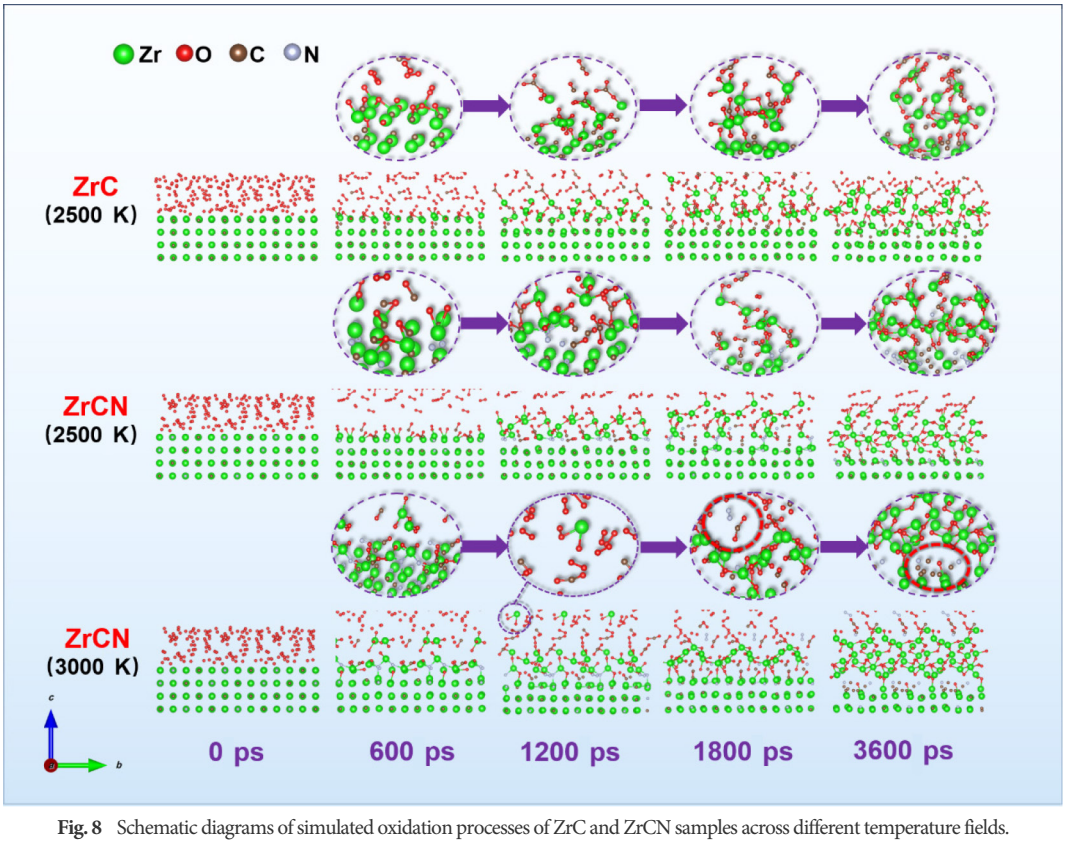

Fig. 8 Schematic diagrams of simulated oxidation processes of ZrC and ZrCN samples across different temperature fields.

reinforce the network structure of the oxide layer, postponing the spallation and liberation of oxidation products and thereby diminishing material loss due to mechanical erosion and chemical degradation. Additionally, nitrogen demonstrates distinct temperature-dependent behavior during the oxidation process, as revealed by molecular dynamics simulations: at 2500 K, it integrates into the oxide network to bolster structural integrity, preventing delamination of the oxide layer. At 3000 K, despite the gradual escape of nitrogen as N_2 gas, the oxide layer network structure retains its integrity. The synergistic mechanisms—including dense oxide layer formation, viscosity modulation, and bonding stabilization—collectively enhance the ultrahigh-temperature ablation resistance of nitrogen-doped ZrC ceramics.

4 Conclusions

In summary, a series of single-phase nitrogen-doped zirconium carbides were successfully synthesized through spark plasma sintering technology. These tailored nitrogen-doped zirconium carbides exhibit superior ablation resistance relative to existing ultrahigh-temperature ceramics. By integrating experimental findings with ab initio molecular dynamics simulations, it has been demonstrated that a dense ablated structure with suitable viscosity in nitrogen-doped zirconium carbide minimizes oxide loss and enhances ablation resistance. Furthermore, nitrogen doping effectively mitigates the discrepancy in the thermal expansion coefficients between the oxide and nonoxide regions. Overall, ultrahigh-temperature nitrogen-doped carbide ceramics hold significant potential for aerospace applications, and these findings may provide critical insights for the advancement of ultrahigh-temperature ceramics.

Acknowledgements

We acknowledge funding by the National Natural Science Foundation of China (No. 52302128) and the Foundation of State Key Laboratory of Science and Technology on Advanced Ceramic Fibers and Composites (No. 6142907230303).

Author contributions

Zheng Peng: Conceptualization, methodology, funding acquisition, analysis, and writing review & editing,and investigation. Yingjie Cui: Sofware, data curation, writing original draft preparation, writing review & editing, and investigation. Jianbo Song: Investigation and conceptualization. Sian Chen: Funding acquisition, validation, and conceptualization. Zengsheng Ma: Investigation and conceptualization. Fuhua Cao: Methodology, investigation

Availability of data and materials

The data that support the findings of this study are available from the corresponding author upon reasonable request.

Competing interests

The authors have no competing interests to declare that are relevant to the content of this article.

References

[1] Li YL, Zhao SJ, Wu ZG. Uncovering the effects of chemical disorder on the irradiation resistance of high-entropy carbide ceramics. *Acta Mater* 2024, **277**: 120187.

[2] Xin XT, Bao WC, Wang XG, *et al.* Reduced He ion irradiation damage in ZrC-based high-entropy ceramics. *J Adv Ceram* 2023, **12**: 916–929.

[3] Suvorova (Buinevich) VS, Nepapushev AA, Moskovskikh DO, *et al.* Fabrication and oxidation resistance of the hafnium carbonitride–silicon carbide composites. *Ceram Int* 2022, **48**: 23870–23877.

[4] Li ZQ, Li HJ, Li W, *et al.* Preparation and ablation properties of ZrC–SiC coating for carbon/carbon composites by solid phase infiltration. *Appl Surf Sci* 2011, **258**: 565–571.

[5] Fahrenholtz WG, Hilmas GE. Ultra-high temperature ceramics: Materials for extreme environments. *Scripta Mater* 2017, **129**: 94–99.

[6] Wang RN, Zhang JP, Liu B, *et al.* Ablation of advanced C/C–ZrC–SiC leading edge composites. *Corros Sci* 2024, **226**: 111648.

[7] Li JC, Zhang YL, Zhao YX, *et al.* A novel $(Hf_{1/3}Zr_{1/3}Ti_{1/3})C$ medium-entropy carbide coating with excellent long-life ablation resistance applied above 2100 °C. *Compos Part B Eng* 2023, **251**: 110467.

[8] Ul-Hamid A. Microstructure, properties and applications of Zr-carbide, Zr-nitride and Zr-carbonitride coatings: A review. *Mater Adv* 2020, **1**: 1012–1037.

[9] Peng Z, Sun W, Xiong X, *et al.* Novel refractory high-entropy ceramics: Transition metal carbonitrides with superior ablation resistance. *Corros Sci* 2021, **184**: 109359.

[10] Frank F, Tkadletz M, Czettl C, *et al.* Microstructure and mechanical properties of ZrN, ZrCN and ZrC coatings grown by chemical vapor deposition. *Coatings* 2021, **11**: 491.

[11] Suvorova V, Khadyrova I, Nepapushev A, *et al.* Fabrication and investigation of novel hafnium-zirconium carbonitride ultra-high temperature ceramics. *Ceram Int* 2023, **49**: 23809–23816.

[12] Valenza TC, Weber PK, Marquis EA. Role of nitrogen in the high-temperature oxidation of titanium alloys. *Corros Sci* 2024, **235**: 112164.

[13] Robin Chang YH, Yoon TL. Effects of nitrogen addition and growth condition on the enhanced mechanical properties of transition metal carbides TMC (TM = Zr, Hf). *Ceram Int* 2020, **46**: 1124–1136.

[14] Farhadizadeh A, Vlček J, Houška J, *et al.* Effect of nitrogen content on high-temperature stability of hard and optically transparent amorphous Hf-Y-Si-B-C-N coatings. *Ceram Int* 2023, **49**: 6086–6093.

[15] Zhang P, Liu XJ, He GY, *et al.* Novel high-entropy ultra-high temperature ceramics with enhanced ablation resistance. *Rare Met* 2024, **43**: 6559–6570.

[16] Peng Z, Sun W, Xiong X, *et al.* Novel nitrogen-doped hafnium carbides for advanced ablation resistance up to 3273 K. *Corros Sci* 2021, **189**: 109623.

[17] Van de Walle A, Asta M, Ceder G. The alloy theoretic automated toolkit: A user guide. *Calphad* 2002, **26**: 539–553.

[18] Kresse G, Furthmüller J. Efficiency of *ab-initio* total energy calculations for metals and semiconductors using a plane-wave basis set. *Comput Mater Sci* 1996, **6**: 15–50.

[19] Kresse G, Hafner J. Ab initio molecular dynamics for liquid metals. *Phys Rev B* 1993, **47**: 558–561.

[20] Kresse G, Furthmüller J. Efficient iterative schemes for *ab initio* total-energy calculations using a plane-wave basis set. *Phys Rev B* 1996, **54**: 11169–11186.

[21] Blöchl PE, Först CJ, Schimpl J. Projector augmented wave method: *Ab initio* molecular dynamics with full wave functions. *Bull Mater Sci* 2003, **26**: 33–41.

[22] Kresse G, Joubert D. From ultrasoft pseudopotentials to the projector augmented-wave method. *Phys Rev B* 1999, **59**: 1758–1775.

[23] Denton AR, Ashcroft NW. Vegard's law. *Phys Rev A* 1991, **43**: 3161–3164.

[24] Vorotilo S, Sidnov K, Mosyagin IY, *et al.* *Ab-initio* modeling and experimental investigation of properties of ultra-high temperature solid solutions $Ta_xZr_{1-x}C$. *J Alloys Compd* 2019, **778**: 480–486.

[25] Smith CJ, Yu XX, Guo QY, *et al.* Phase, hardness, and deformation slip behavior in mixed $Hf_xTa_{1-x}C$. *Acta Mater* 2018, **145**: 142–153.

[26] Lengauer W, Binder S, Aigner K, *et al.* Solid state properties of group IVb carbonitrides. *J Alloys Compd* 1995, **217**: 137–147.

[27] Zeng Y, Wang DN, Xiong X, *et al.* Ablation-resistant carbide

$Zr_{0.8}Ti_{0.2}C_{0.74}B_{0.26}$ for oxidizing environments up to 3,000 °C. *Nat Commun* 2017, **8**: 15836.

[28] Tang ZY, Wen ZH, Liu YW, *et al.* Rapid experimental screening of high-entropy diborides for superior oxidation resistance. *Adv Funct Materials* 2024, **34**: 2312239.

[29] Yan CL, Luo P, Zhang JJ, *et al.* Ablation behavior of C_f/ZrC–SiC ultra–high temperature ceramic composites in oxyacetylene torch and plasma wind tunnel. *Mater Today Commun* 2024, **41** : 110477.

[30] Yu Y, Jiang BH, Liu W, *et al.* Fabrication and ablation resistance research of C/ZrC–SiC composites. *IOP Conf Ser: Mater Sci Eng* 2020, **733**: 012016.

[31] Liao HY, Zhou Z, Dai CY, *et al.* SPS densification and ablative performance of ZrB_2–SiC–ZrC composites derived from the ternary powders by sol-gel. *Ceram Int* 2023, **49**: 17709–17718.

[32] Pan XH, Niu YR, Xu XT, *et al.* Long time ablation behaviors of designed ZrC–SiC–TiC ternary coatings for environments above 2000 °C. *Corros Sci* 2020, **170**: 108645.

[33] Cheng Y, Liu C, Hu P, *et al.* Using *in situ* conversed nano SiC to bond UHTC particles and construct anti-ablation coating. *Compos Part A Appl Sci Manuf* 2022, **162**: 107159.

[34] Lyu Y, Cheng Y, Zhao GD, *et al.* Modification of SiBCN by Zr atom and its effect on ablative resistance of C_f/SiBCN(Zr) composites. *Compos Part B Eng* 2023, **253**: 110511.

[35] Lyu Y, Han ZH, Zhao GD, *et al.* Efficient fabrication of light C_f/SiHfBOC composites with excellent thermal shock resistance and ultra-high-temperature ablation up to 1800 °C. *J Adv Ceram* 2023, **12**: 2062–2074.

[36] Zou J, Rubio V, Binner J. Thermoablative resistance of ZrB_2–SiC–WC ceramics at 2400 °C. *Acta Mater* 2017, **133**: 293–302.

[37] Scott JA, He XQ, Lipke DW. The role of microstructure on high-temperature oxidation behavior of hafnium carbide. *J Am Ceram Soc* 2023, **106**: 3116–3126.

[38] Hakeem AS, Wójcik NA, Wolff S, *et al.* Evaluating the impact of ZnO doping on electrical and thermal properties of calcium-aluminosilicate oxynitride glass-ceramics. *Ceram Int* 2024, **50**: 37665–37675.

[39] Ye ZM, Zeng Y, Xiong X, *et al.* Elucidating the role of preferential oxidation during ablation: Insights on the design and optimization of multicomponent ultra-high temperature ceramics. *J Adv Ceram* 2022, **11**: 1956–1975.

[40] Ye ZM, Zeng Y, Xiong X, *et al.* Revealing the solid-state reaction process among multiphase multicomponent ceramic during ablation. *Adv Powder Mater* 2024, **3**: 100189.

[41] Backman L, Gild J, Luo J, *et al.* Part I: Theoretical predictions of preferential oxidation in refractory high entropy materials. *Acta Mater* 2020, **197**: 20–27.

[42] Li YL, He L, Pan H, *et al.* Compositional optimization for enhanced oxidation resistance of high-entropy carbide ceramics. *Acta Mater* 2025, **282**: 120463.